Journal of Quantitative Spectroscopy & Radiative Transfer 246 (2020) 106920

Contents lists available at ScienceDirect

Journal of Quantitative Spectroscopy & Radiative Transfer

journal homepage: www.elsevier.com/locate/jqsrt

Using polarimetric observations to detect and quantify the three-dimensional radiative transfer effects in passive satellite cloud property retrievals: Theoretical framework and feasibility study

Chamara Rajapakshe[a], Zhibo Zhang[a,b,*]

[a] Physics Department, UMBC, Baltimore, Maryland
[b] Joint Center for Earth Systems Technology, UMBC, Baltimore, Maryland

ARTICLE INFO

Article history:
Received 23 September 2019
Revised 10 February 2020
Accepted 19 February 2020
Available online 26 February 2020

1. Introduction

Clouds play an important role in the earth systems. To better understand this role and simulate clouds in the numerical weather and climate models requires observations of cloud properties from regional to global scales. Many satellite remote sensing techniques have been developed to meet this requirement. Of particular interest in this study is the cloud optical thickness (COT) retrievals from the passive satellite observations of cloud reflectance in the visible (VIS) or near-infrared (NIR) band. The COT is an important cloud parameter that largely determines the radiative effects of clouds. A widely used method for COT retrieval is simultaneously retrieving the COT with cloud effective radius (CER) based on a pair of observed cloud reflectances, one in VIS/NIR spectral region and the other in the water-absorbing shortwave infrared region (SWIR) [1]. This so-called bi-spectral method has been adopted in several widely used operational cloud products, such as MODIS (Moderate Resolution Imaging Spectroradiometer), VIIRS (Visible Infrared Imaging Radiometer Suite) and SEVIRI (Spinning Enhanced Visible and Infrared Imager) [2–4]. The retrievals that utilizes the multangular polarimetric observations for cloud microphysics retrievals is another widely used approach which exploits the angular pattern of the polarimetric cloud reflectances in the cloud bow scattering angles [5,6]. This method not only provides retrievals of CER but also estimates the width of cloud droplet size distribution (i.e., cloud effective variance (CEV) of cloud top droplet size distribution). The polarimetric based cloud microphysics retrievals (polarimetric retrieval for short) have been used for the POLDER satellite mission, as well as several airborne polarimeters such as RSP (Research Scanning Polarimeter), airMSPI (Airborne Multiangle SpectroPolarimetric Imager) and airHARP (Airborne Hyper-Angular Rainbow Polarimeter) [7–9].

Most operational passive satellite cloud remote sensing algorithms, including those mentioned above, are based on 1-D Radiative Transfer (RT) theory, which makes two fundamental and important assumptions. The first assumption, often referred to as the "plane-parallel approximation" (PPA), assumes cloud fields within each cloudy pixel to be horizontally homogeneous. The second assumption is known as the "independent pixel approximation" (IPA) that assumes all pixels are independent of each other from the perspective of net photon transportation. In some situations, such as stratus clouds, these assumptions are not unreasonable. However, in many other circumstances, clouds have distinct 3-D structures that deviate substantially from the above two assumptions. In such cases, cloud radiative properties (e.g., reflectance and transmittance) determined by 3-D RT would be different from those derived based on 1-D RT theory. As a result, the operational passive remote sensing algorithms, which uses the 1-D RT theory to interpret the observed cloud radiative properties, are subjected to significant biases and uncertainties. This is known as the "3-D radiative transfer effect" in passive cloud remote sensing. Hence, the 3-D radiative effect is a fundamentally inherited challenge, not only in operational cloud property retrievals but also in various remote sensing applications other than the techniques that involve line-of-sight absorption and emission with little atmospheric scattering [10–12].

The 3-D RT effects in cloud property retrievals may have various adverse implications. For example, satellite retrievals are an important source of data for global cloud property observations, which are especially valuable for evaluating and improving global climate

* Corresponding author.
E-mail address: zhibo.zhang@umbc.edu (Z. Zhang).

https://doi.org/10.1016/j.jqsrt.2020.106920

models. However, biases and uncertainties caused by the 3-D effects can complicate the evaluation process and even mislead the conclusions [13,14]. Furthermore, the studies on the aerosol indirect effects that use the observed relationship between the aerosol amount and cloud properties [15–17] could also be affected by the 3-D radiative effects in passive cloud property retrievals [10] .

In the past, most research has focused on elucidating the physics behind the 3-D RT effects and assessing the consequential impacts on the retrieved cloud properties, such as cloud optical thickness [12,18–20] and cloud effective radius [10,21,22]. Thanks to these studies, we now have a reasonable understanding of what conditions would favor the 3-D RT effect (e.g., broken clouds under the low sun condition), which enables us to filter the satellite cloud property retrievals to reduce the impact of 3-D radiative effect. For example, passive cloud property retrievals in the high-latitude regions are often disregarded all together in many model evaluation studies partly due to the concern of enhanced 3-D RT effect under the low sun conditions (e.g., [23–25]). Obviously, such crude filtering causes a significant data loss. Pixel-level identification of 3-D RT effect is certainly more ideal, but unfortunately it has been proven to be a highly challenging problem. Some studies attempted to use the sub-pixel inhomogeneity as an index for 3-D RT effect (e.g., [22,26,27]). The limitation of the sub-pixel inhomogeneity index is, it only can be used to identify the violation of the PPA but not IPA. As explained in Section 3, as well as many previous studies, the violation of IPA can lead to some strong 3-D RT effects (e.g., illuminating and shadowing effect) and thereby cause large errors in retrieved COT and CER. Some attempts have been made to identify the 3-D RT effects caused by the violation of the IPA. For example, Várnai and Marshak [28] used the cloud top topography retrievals based on the infrared cloud observations that are minimally affected by the 3-D RT effect to identify the pixels influenced by the illuminating and shadowing effects in the visible band. Their method clearly revealed that the COT retrievals influenced by the illuminating effects are statistically larger than those influenced by the shadowing effect. Nevertheless, this method faces two limitations. First, although it can be useful to identify the pixels influenced by the 3-D RT effect, it cannot be used to quantitively correct the COT retrieval bias. Second, the method involves rather complicated multi-pixel analysis which makes it difficult to implement as an operational algorithm. Lately, some attempts have been made to use the machine-learning techniques to retrieve the cloud properties based on the 3-D, instead of the 1-D RT theory. A common theme of these studies is to first develop a large collection of synthetic satellite cloud observations based on simulated cloud fields (e.g., from a large-eddy-simulation model) and 3-D RT model. Then the simulated samples are used to train the machine-learning algorithm which will be in turn used to retrieve the cloud properties from the real observations. These methods are still at their infancy and their performance, especially applied to real data, need further studies.

In this study, we explore a new method based on the physical principles of RT and utilize the unique capability of multi-angular polarimetric cloud observation to both identify and correct the 3-D radiative effect. In particular, our method, referred to as the "maximum 1-D reflectance method", is highly effective and efficient to detect the pixels influenced by strong illuminating effect. The outline of this paper, as follows. First, Section 2 provides a brief description about the hypothetical 1-D cloud fields and the radiative transfer simulation model that have been used. Then, Section 3 uses one hypothetical cloud field to explain how the 3-D RT effects appear at the cloud property retrievals. Thereafter, Section 4 introduces a quantity called 3-D effect impact factor. After that, Section 5 explains our "maximum 1-D reflectance" mainly emphasizing the capability of detecting illuminating effects. Section 6 further explores the maximum 1-D reflectance method towards correcting COT biases. Stepwise procedure of implementation is mentioned at the beginning of Section 5 by summarizing both Section 5 and 6. Section 7 discusses about potential observational implementation for future studies and Finally, Section 8 gives a summary and offers some concluding remarks.

2. Models

In this study, two hypothetical 1-D cloud fields have been used. The first one is referred to "step cloud" (Fig. 1 (a)) which has a constant physical thickness of 1 km and an optically thick region (COT = 10.0) at the middle surrounded by two optically thin regions (COT = 0.1) at each edge. The cloud effective radius of the step cloud is assumed to be 10 μm. Though the step cloud case is very useful to demonstrate and understand certain physical principles, it is too simple from realistic cloud fields. Hence we will use the well-known fractal cloud generation method, the bounded cascade model [29] to generate our second hypothetical 1-D cloud field which is hereafter referred as the "fractal cloud" for short.

Fig. 3 (a) shows the fractal cloud field simulated based on the bounded cascade model [29]. This model uses a two-parameter multiplicative recurrent process that allows simulating the realistic horizontal spatial distribution of the cloud liquid water path (LWP) when the mean LWP is known [30,31]. The modeling process starts with a uniform plane-parallel cloud slab with a constant mean LWP. This initial cloud slab has a finite geometrical thickness Δz and Δx, but infinite along the y direction. The recursive procedure proceeds as follows: Divide the uniform slab into two halves (i.e., $\Delta x/2$) at the middle of the x dimension, and then transfer f_0 fraction of water mass from one side to the other chosen randomly with equal probability. Subsequently, each of the new halves is treated as two separate slabs and sub-divide each into two halves and transfer f_1 fraction of water among adjacent halves again chosen randomly with equal probability. This process continues multiple times to produce fractal-like LWP variation along the x dimension. The n^{th} fractional mass is specified by

$$f_n = f_0 c^n \tag{1}$$

where scaling parameter c and the variance parameter f_0 are set to be $2^{-1/3}$ and 0.5, respectively, to follow LWP distribution characteristics of a stratocumulus cloud [29] . The mean LWP of the cloud was set to be 90 g/m^2. The effective radius and effective variance are 12 μm and 0.05 respectively. The horizontal resolution, i.e., the final grid size, along the x-axis is 10 m. Periodical boundary conditions are used in RT simulations. Note that the Mie calculations for this study are computed using Wiscombe [32] Mie code and the well-known modified gamma distribution [33] is assumed as the droplet size distribution in the bulk optical property computations.

Both 3-D and 1-D radiative transfer simulations for this study were performed using the Multiple-Scaling-based Cloudy Atmospheric Radiative Transfer (MSCART) model [34,35]. When the medium has a highly forward-peaked scattering phase function such as in cloud droplets and ice crystals, the variance of the simulated radiances in a Monte-Carlo method increases dramatically which costs large amounts of photons and thereby computational time to reach sufficient accuracy. Many previous RT simulation models have used either the phase function forward truncation method or the target directional importance sampling technique for radiance variance reduction. In the phase function forward truncation method, the photons that are scattered into the highly forward-peak direction are "forcefully" considered as not being scattered at all. Then to compensate the truncated forward-peak, the single scattering albedo and the optical thickness of the medium are adjusted [36–38]. The target directional importance sampling technique computes the probability that a photon will be scattered towards the sensor at each scattering event while trac-

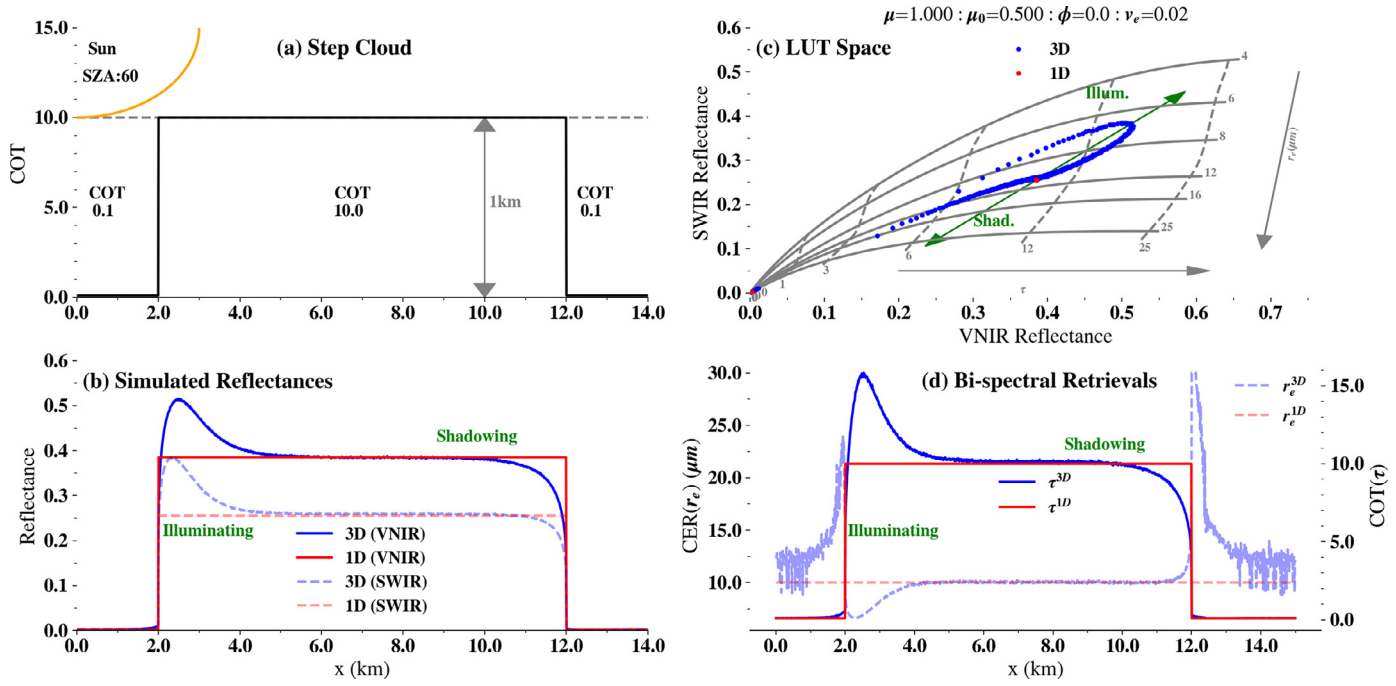

Fig. 1. (a) An idealized 1-D cloud field named the "step cloud". (b) Simulated 1-D and 3-D VNIR reflectances (solid red and blue respectively) and 1-D and 3-D SWIR reflectances (dashed red and blue respectively) for (a). (c) The illuminating and shadowing effects in (b) depicted in the bi-spectral LUT space (SZA = 60°, VZA = 0, CEV = 0.02). (d) The cloud optical thickness and the cloud effective radius retrievals based on (c). (For interpretation of the references to color in this figure legend, the reader is referred to the web version of this article.)

ing the photon path to improve the efficiency [39]. Different from these previous studies, MSCART uses a novel hybrid scattering-order dependent variance reduction method which combines the phase function forward truncation technique together with the target directional importance sampling technique at each scattering order to maintain the optimal balance between numerical efficiency and accuracy.

3. Illuminating and shadowing effects

As aforementioned, IPA is one among the two fundamental assumptions of the 1-D RT theory. However, when the cloud field has significant horizontal variability, either optically or geometrically, the net horizontal transport of photon can lead to the violation of IPA and thereby 3-D RT effects. The so-called illuminating and shadowing effects are classic examples of such 3-D RT effects. Here, we use idealized "step-cloud" example to illustrate 3-D RT effects and their impacts on the bi-spectral retrievals of COT and CER. As shown in Fig. 1 (a) the "step cloud" case, If the cloud is illuminated from the left-hand side at solar zenith angle (SZA) = 60°, the resultant simulated reflectances for both VNIR (visible and near-infrared) and SWIR (shortwave infrared) bands are shown in Fig. 1(b). The solid and dashed red lines are VNIR and SWIR reflectances respectively based on 1-D radiative transfer simulations. The solid and dashed blue lines are VNIR and SWIR reflectances respectively based on 3-D radiative transfer simulations. (Note that, the same color convention, which is red for 1-D and blue for 3-D RT-based results, is adopted in all figures).

As a result of IPA, the simulated cloud reflectance based on the 1-D RT theory is simply a step function that follows the variation of COT. Interestingly, the cloud reflectances simulated based on the 3-D RT theory are quite different, especially at the transition regions (e.g., from thin to thick or from thick to thin). At the illuminating side (i.e., 2–4 km), the cloud reflectances simulated based on 3-D RT theory (hereafter referred to as "3-D cloud reflectance" for short) are significantly larger compared to their 1-D counterparts. This is known as the "illuminating effect" which is caused by the photon transfer from the optically thin region to the optically thick region due to the multiple scattering. In contrast, at the shadowing edge, (i.e., 10–12 km) the photon leaking from optically thick region to optically thin region causes a significant drop in the 3-D reflectances compared to the 1-D reflectances which is called the "shadowing effect". In general, at the illuminating side, both VNIR and SWIR reflectances increase due to 3-D RT effects and both decrease at the shadowing side.

Fig. 1(c) illustrates how these 3-D RT effects influence the bi-spectral retrieval in Nakajima-King LUT (Look-up table) space [1]. Since the 1-D cloud reflectances are step functions, they simply reduce to two points in the LUT space. One point corresponding to the thin part of the step cloud is located at the lower left corner close to the origin of the LUT. The other corresponding to the thick part is located at the center of the LUT with VNIR and SWIR reflectance around 0.39 and 0.25, respectively. In case of the illuminating effect, the 3-D cloud reflectances are larger and therefore located to the upper right of the 1-D cloud reflectances in the LUT space. As a result of the shadowing effect, the 3-D cloud reflectances are smaller and therefore located to the lower left of the 1-D cloud reflectances in the LUT space. Therefore, as shown in Fig. 1 (d), the illuminating effects cause positive biases in COT retrievals and negative biases in CER retrievals while the shadowing effects cause negative biases in COT and positive biases in the CER.

Fig. 2 (a) shows the simulated VNIR polarized reflectance (i.e., $R_Q = \pi Q/(\mu_0 F_0)$ where Q is the second component of the reflected Stoke Vector, $\mu_0 F_0$ is the incident flux) for the step cloud case. The solid blue line is VNIR polarized reflectance from 3-D RT simulations and the solid red line is VNIR polarized reflectance from 1-D RT simulations. For the same band, polarized reflectance has sharp illuminating and shadowing effects compared to those in the total reflectances in Fig. 1 (b). It is important to note that, even though the magnitude of the polarized reflectance vary at the illuminating (x =2.11 km) and shadowing (x = 11.95 km) edges compared to the middle of the cloud (x = 6.01), as shown in Fig. 2 (b),

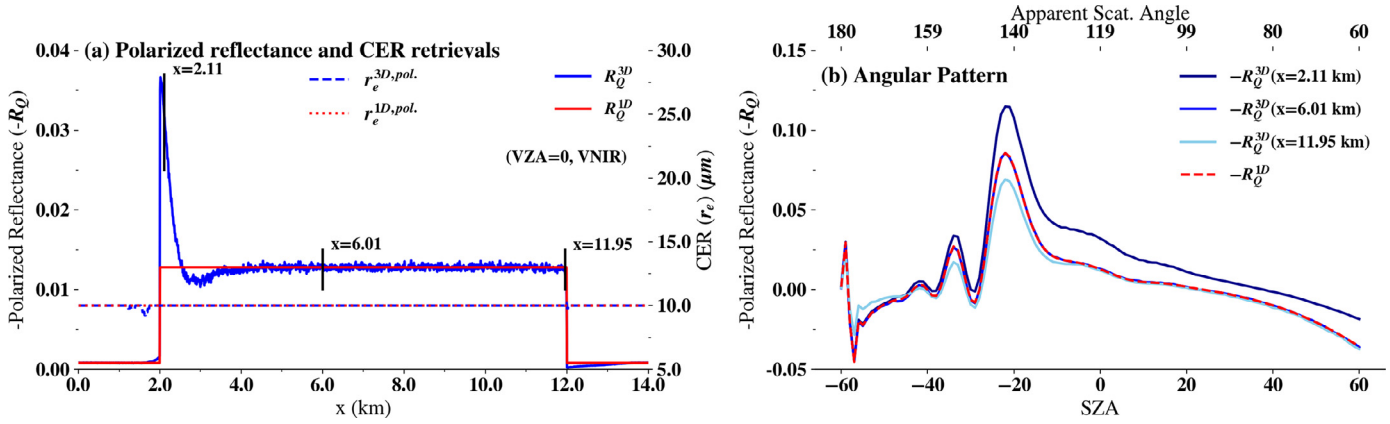

Fig. 2. (a) Simulated polarized reflectances for the step cloud case in Fig. 1 (a) based on 3-D and 1-D RT simulations (blue and red solid lines respectively) at VZA = 0 for VNIR band. Corresponding polarimetric CER retrievals are shown in blue dashed and red dotted lines based on 3-D and 1-D RT-based polarized reflectance respectively. (b) Angular pattern of the polarized reflectance at the selected locations (x = 2.11, 6.01 and 11.95 km) in (a). (For interpretation of the references to color in this figure legend, the reader is referred to the web version of this article.)

the angular pattern remains mostly unchanged. Note that different from the bi-spectral CER retrievals which are based on the magnitudes of the total reflectances, the polarimetric CER retrievals rely upon the angular pattern of the polarized reflectances. Hence the magnitude change in the polarized reflectance due to the 3-D effects has a negligible influence on the underlying CER retrievals. This feature is evident in CER retrievals shown in Fig. 2 (a), where the polarimetric retrievals of CER ($r_e^{pol.}$) from both 1-D and 3-D RT simulations (dotted red and dashed blue line respectively) are almost identical regardless the illuminating and shadowing effects. After further investigations, we exploit this interesting advantage of the polarimetric retrieval technique for our "maximum 1-D reflectance method" in Section 5.

4. 3-D Effect impact factor

The step cloud case is useful for introducing main concepts and revealing the underlying physics, but it is too simple and ideal. To establish and test our method in more realistic conditions, in this section we will use the well-known fractal cloud field to further illustrate the illuminating and shadowing, and also to explain our "maximum 1-D reflectance method" for 3-D RT effect detection and correction.

Fig. 3(b) shows 1-D and 3-D SWIR band (i.e., 2.13 μm) reflectances simulated using the MSCART model in red and blue respectively for the nadir viewing geometry. The sun is to the left at SZA = 60º. One can see from the figure, whenever there is an abrupt variation in COT, e.g., around 11 km and 21 km, the illuminating and shadowing effects are clearly observable. To quantify how strong the 3-D effect, we define a quantity called "3-D effect impact factor" as follows

$$f_{R_\lambda} = \frac{R_\lambda^{3D} - R_\lambda^{1D}}{R_\lambda^{1D}} = \frac{\Delta R}{R_\lambda^{1D}}; \lambda = \{SWIR, VNIR\} \quad (2)$$

Where R_λ^{3D} and R_λ^{1D} are the 3-D and 1-D reflectance, respectively. The SWIR 3-D effect impact factor ($f_{R_{SWIR}}$) derived based on the simulated SWIR reflectances (R_{SWIR}^{3D}, R_{SWIR}^{1D}) of the fractal cloud case for SZA = 60º is shown in the black curve in Fig. 3 (c). Clearly, the positive 3-D effect impact factors ($f_\lambda > 0$) indicate the illuminating effects while the negative values ($f_\lambda < 0$) indicate the shadowing effects. In other words, the sign and magnitude of the f_{R_λ} can be used to detect and quantify the illuminating and shadowing effects. Moreover, if the f_λ is known for a observed 3-D cloud reflectance, Eq. (2) can be used to obtain corresponding unbiased R_λ^{1D} ($R_\lambda^{1D} = R_\lambda^{3D}/(1+f_\lambda)$). The grey curve in Fig. 3 (c) is the 3-D effect impact factor for SZA = 40º. While acknowledging the necessity of further investigations based on more realistic cloud fields in the future studies, here we can qualitatively observe that the strength of 3-D effects (both illuminating and shadowing) decreases as SZA decreases.

5. Maximum 1-D reflectance method to detect illuminating effect

As mentioned in the last section, the sign and the magnitude of the f_{R_λ} can be used to detect the 3-D effect and assess its strength. Note that the observed cloud reflectance R_λ^{3D} is inherently a result of 3-D radiative transfer. Therefore, the key problem is how to estimate the 1-D cloud reflectance R_λ^{1D}. Unfortunately, it is an extremely challenging task to obtain the R_λ^{1D} for all pixels under all circumstances. And, it is *not* our objective. Instead, our method focuses on the pixels that are strongly influenced by the illuminating effect.

The step-by-step procedure for implementing the maximum 1-D reflectance method to detect and correct strong illuminating effects as follows. Fig. 6 shows the flowchart. The detection process is shown in solid lines and the correction process is shown in dashed lines. The detection and correction processes are explained in detail in Section 5 and Section 6 respectively.

1. Use the r_e^{pol} retrieved from the polarized reflectance as the "true" CER.
2. Select the corresponding SWIR-VNIR theoretical relationship ($g_{LUT}^{r_e=r_e^{pol}}$) for r_e^{pol} from the LUT and select a VNIR reflectance threshold (R_{VNIR}^*) such that the gradient of the SWIR-VNIR theoretical relationship $[\frac{dR_{SWIR}}{dR_{VNIR}}]^{r_e=r_e^{pol}}$ is smaller than 0.01 (ideally approaches to zero). Subsequently obtain the maximum possible SWIR reflectance, $R_{SWIR}^{1D,max}(r_e^{pol})$ and assume assume $R_{SWIR}^{1D,max}$ as the R_{SWIR}^{1D} for all the observations that $R_{VNIR}^{3D} > R_{VNIR}^*$ (Eq. 3).
3. Use Eq. (2) and Eq (3) to get the 3-D effect impact factor of the SWIR band, $f_{R_{SWIR}}^{apx.}$.
4. Assume both VNIR and SWIR 3-D effect impact factors are approximately equal (Eq. (4)).
5. Use $f_{R_{SWIR}}^{apx.}$ *and* $f_{R_{VNIR}}^{apx.}$ to correct both SWIR and VNIR reflectances respectively for all the observations that $R_{VNIR}^{3D} > R_{VNIR}^*$ (By using, $R_\lambda^{1D} = R_\lambda^{3D}/(1+f_{R_\lambda}^{apx})$).
6. Use the corrected reflectances to do bi-spectral retrievals.

We argue that, if the observed R_λ^{3D} for a target pixel is even larger than the maximum value of cloud reflectance that is al-

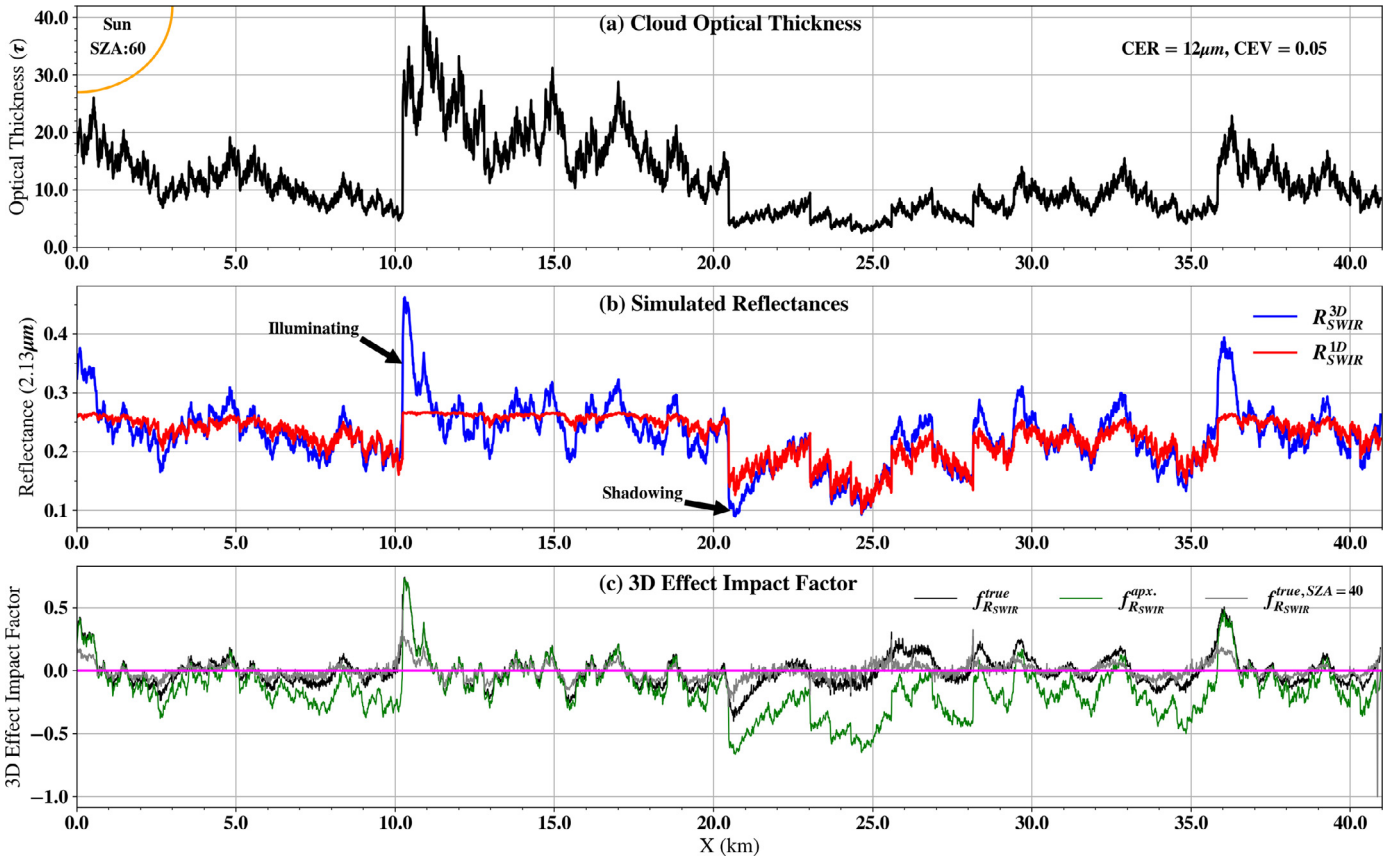

Fig. 3. (a) The cloud optical thickness variation of the fractal cloud generated from the bounded cascade model. The mean LWP, CER and CEV are 90 g/m^2,12 μm and 0.05 respectively. (b) The simulated SWIR reflectances from 1-D (red) and 3-D (blue) RT-based simulations at SZA = 60° and VZA = 0°. (c) The actual (black) and approximated (green) 3-D effect impact factors of the SWIR band. The grey line is the actual 3-D effect impact factor of the SWIR band for SZA = 40°. (For interpretation of the references to color in this figure legend, the reader is referred to the web version of this article.)

lowed by the 1-D RT theory, then this pixel must be influenced by the illuminating effect. The basic idea of our method can be readily appreciated from Fig. 3(b). Focusing on the R^{1D}_{SWIR} (red line) in the figure, one can notice that no matter how optically thick the cloud is, the R^{1D}_{SWIR} never exceeds certain maximum value, i.e., around 0.27 in this case (see around 10~20 km). This maximum value $R^{1D,max}_{SWIR}(r_e)$ is a result of the absorption of the SWIR band and it is mainly a function of CER (i.e., the larger the CER the smaller the $R^{1D,max}_{SWIR}$). Therefore, if the CER is known, then the maximum 1-D reflectance can be estimated and used to detect the strong illuminating effect.

However, how to estimate the CER of the target cloud still remains as a challenge. As shown in the step cloud case as well as many previous studies, the CER retrieval from the bi-spectral method can be significantly biased due to the 3-D effect and therefore cannot be used. This is where the polarimetric retrievals becomes useful. As explained in Section 3 with the aid of Fig. 2 (b), although the magnitude of the polarimetric cloud reflectance is influenced by 3-D effect, the angular features of the cloud bow remain unchanged. As a result, the retrieved CER from the multi-angular polarimetric observation is minimally affected by the 3-D effects and, hence provides the basis to estimate the maximum 1-D reflectance. In the rest of this section and the proceeding section, we will provide a step-by-step explanation of our method. The stepwise procedure is listed at the begining of this section and a flowchart for practical implementation is provided in Fig. 6.

The first step of the maximum 1-D reflectance method is to estimate the CER of the target cloud field. Fig. 4 (a) shows the simulated polarized reflectances for the fractal cloud case in Fig. 3 (a) based on 1-D (solid red) and 3-D (solid blue) RT simulations for the VNIR band at VZA = 0. We can clearly see the illuminating and shadowing effects near $x \sim 11\,km$ and $x \sim 21\,km$ respectively similar to the simulated total reflectance in Fig. 3 (b). Fig. 4 (b) shows the CER retrievals from both bi-spectral (blue dashed line) and polarimetric (blue solid line) retrieval techniques based on 3-D RT simulations (without applying any corrections). We can clearly see, even though the bi-spectral CER retrievals have strong biases due to the 3-D RT effects, the polarimetric retrievals are mostly around 12 μm within fractions of a micron. Usually, in practice, the polarized reflectance has to be averaged over a coarser spatial domain to cover complete angular space of the cloud bow region in order to implement polarimetric retrieval technique. By takin this into consideration, if we use the domain averaged polarized reflectance to do the retrievals, we get $CER = 12.00\ \mu m$, which is same as the assumed value in the process of fractal cloud generation. In summary, since the polarimetric CER retrievals are minimally affected by 3-D RT effects, we can use the retrieved r_e^{pol} based on the polarized reflectance to approximate the CER of the target cloud.

After obtaining the r_e^{pol} from the polarimetric observations, the next key step is to determine the maximum 1-D reflectance ($R^{1D,max}_{SWIR}(r_e)$) correspond to the retrieved CER. Note again that, this is the maximum cloud reflectance in the SWIR band allowed by the 1-D RT theory. Therefore, any observed cloud reflectance that is larger than this $R^{1D,max}_{SWIR}(r_e)$ is likely affected by the illuminating effect. Fig. 5(a) shows the Nakajima-King (NK) LUT for SZA = 60° and VZA = 0°, in which each solid and dashed isolines correspond to a constant CER ($g^{r_e=r_e^*}_{LUT}$) and a constant COT ($g^{\tau=\tau^*}_{LUT}$), respectively. For a given CER, as the cloud becomes optically thicker with increasing

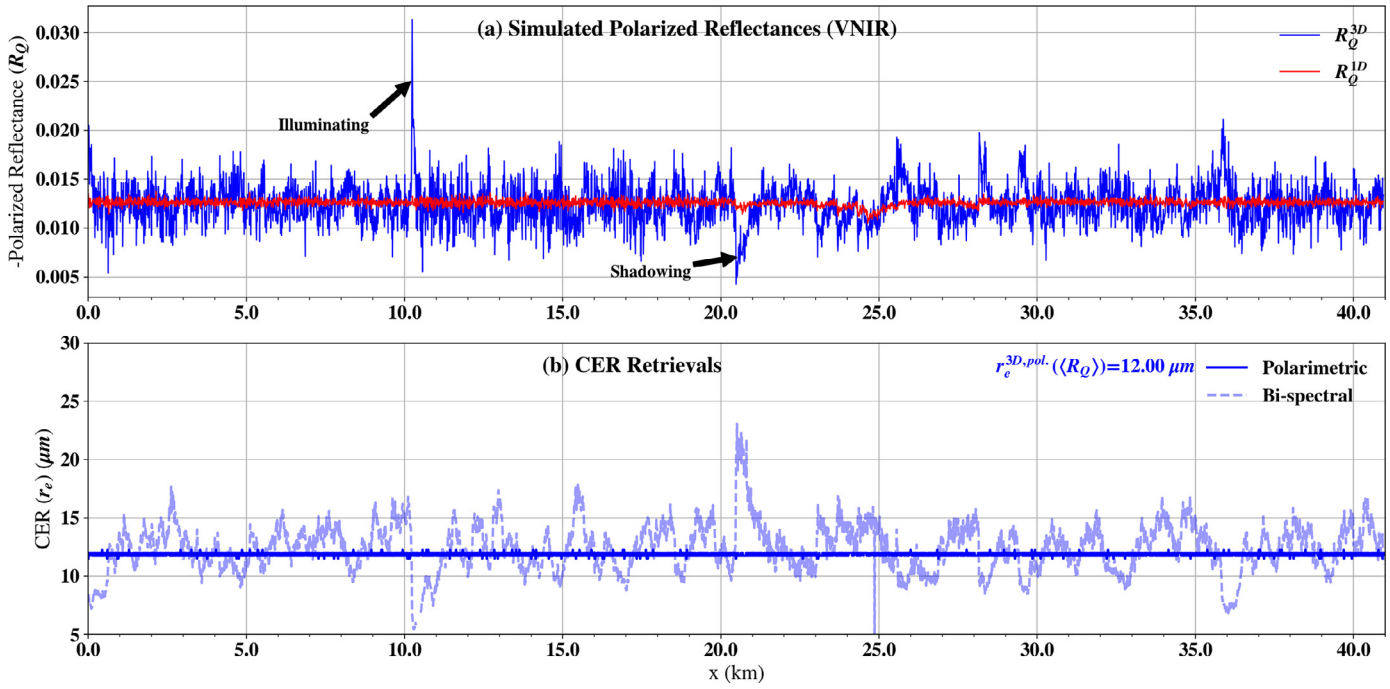

Fig. 4. (a) Simulated 1-D (solid red) and 3-D (solid blue) polarized reflectances for the fractal cloud case in Fig. 3 (a). (b) CER retrievals from bi-spectral (dashed blue) and polarimetric (solid blue) retrieval techniques based on 3-D RT simulations. (For interpretation of the references to color in this figure legend, the reader is referred to the web version of this article.)

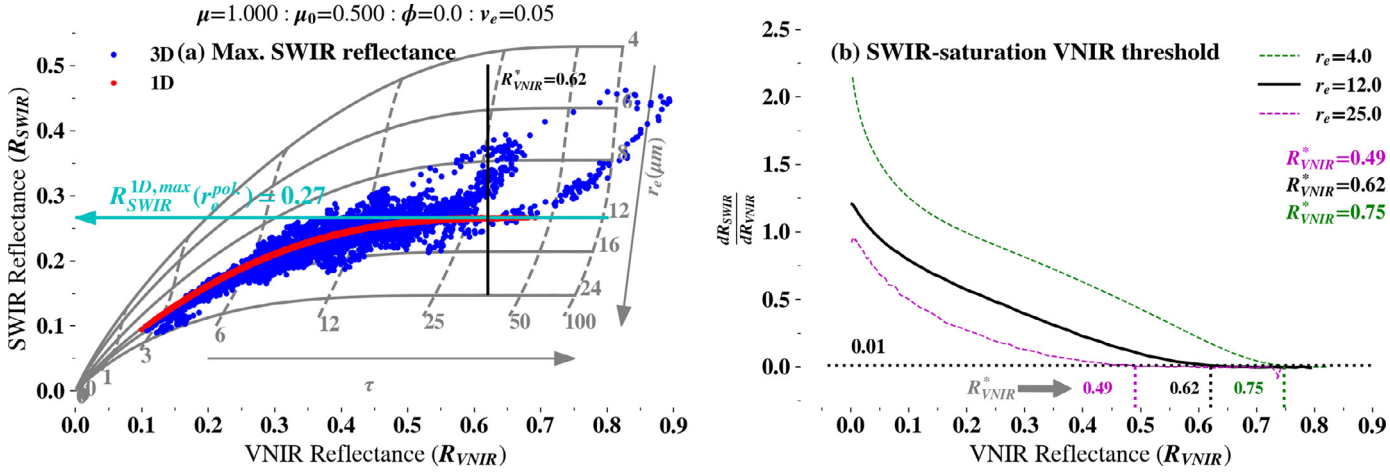

Fig. 5. An illustration of implementing the maximum 1-D reflectance method for the fractal cloud in Fig. 3(a). (a) The theoretical relationships between VNIR and SWIR reflectances for various COT and CER (bi-spectral LUT space) are shown in grey for SZA = 60° and VZA = 0°. The red and blue data points are based on 1-D and 3-D RT simulations respectively for the fractal cloud. Cyan arrow is the maximum possible SWIR reflectance for CER = 12 μm. (b) The variations of the gradients of the constant CER curves for different cloud effective radii. The black horizontal line in (a) is the VNIR threshold based on the gradient of CER = 12 μm curve (black curve). (For interpretation of the references to color in this figure legend, the reader is referred to the web version of this article.)

COT, the SWIR reflectance first increases but eventually reaches to an asymptotic maximum value, i.e., $R^{1D,max}_{SWIR}(r_e)$. The determination of this saturated SWIR reflectance $R^{1D,max}_{SWIR}(r_e)$ from the observed quantities is not trivial and can be done as follows. Qualitatively, one can see in Fig. 5 (a), for a given CER, R^{1D}_{SWIR} reaches $R^{1D,max}_{SWIR}$ when R^{1D}_{VNIR} becomes large enough. Therefore, when the CER is known from the polarimetric retrievals, $R^{1D,max}_{SWIR}$ can be deduced by using $g^{r_e=r_e^{pol.}}_{LUT}$ isoline from the appropriate LUT. To this end, we can define a SWIR-saturated VNIR reflectance threshold (R^*_{VNIR}) based on the slope of the constant CER curve, $[\frac{dR_{SWIR}}{dR_{VNIR}}]^{r_e=r_e^{pol}}$ such that the slope approaches to zero (i.e., R^{1D}_{SWIR} approaches to $R^{1D,max}_{SWIR}$) when $R^{3D}_{VNIR} > R^*_{VNIR}$. Fig. 5(b) shows the gradients of the constant CER curves for three cloud effective radii. The green dashed line, black solid line, and magenta dashed line are for CER= 4.0, 12.0 and 25.0 μm, respectively. As CER increases the gradient of the constant CER curve reaches to zero faster (at a lower VNIR reflectance). Hence the VNIR filtering threshold (R^*_{VNIR}) would be smaller for larger CER (for a given geometry and CEV). In practice the threshold value R^*_{VNIR} can be precomputed based on the LUT. The underlying physics is simple: if the observed R^{3D}_{VNIR} is larger than R^*_{VNIR} then the cloud optical thickness is large enough to saturate the SWIR reflectance, hence the R^{1D}_{SWIR} should approach to $R^{1D,max}_{SWIR}$ i.e.,

$$R^{1D}_{SWIR} \approx R^{1D,max}_{SWIR}\left(r_e^{pol.}\right);\ \ when\ R^{3D}_{VNIR} > R^*_{VNIR} \tag{3}$$

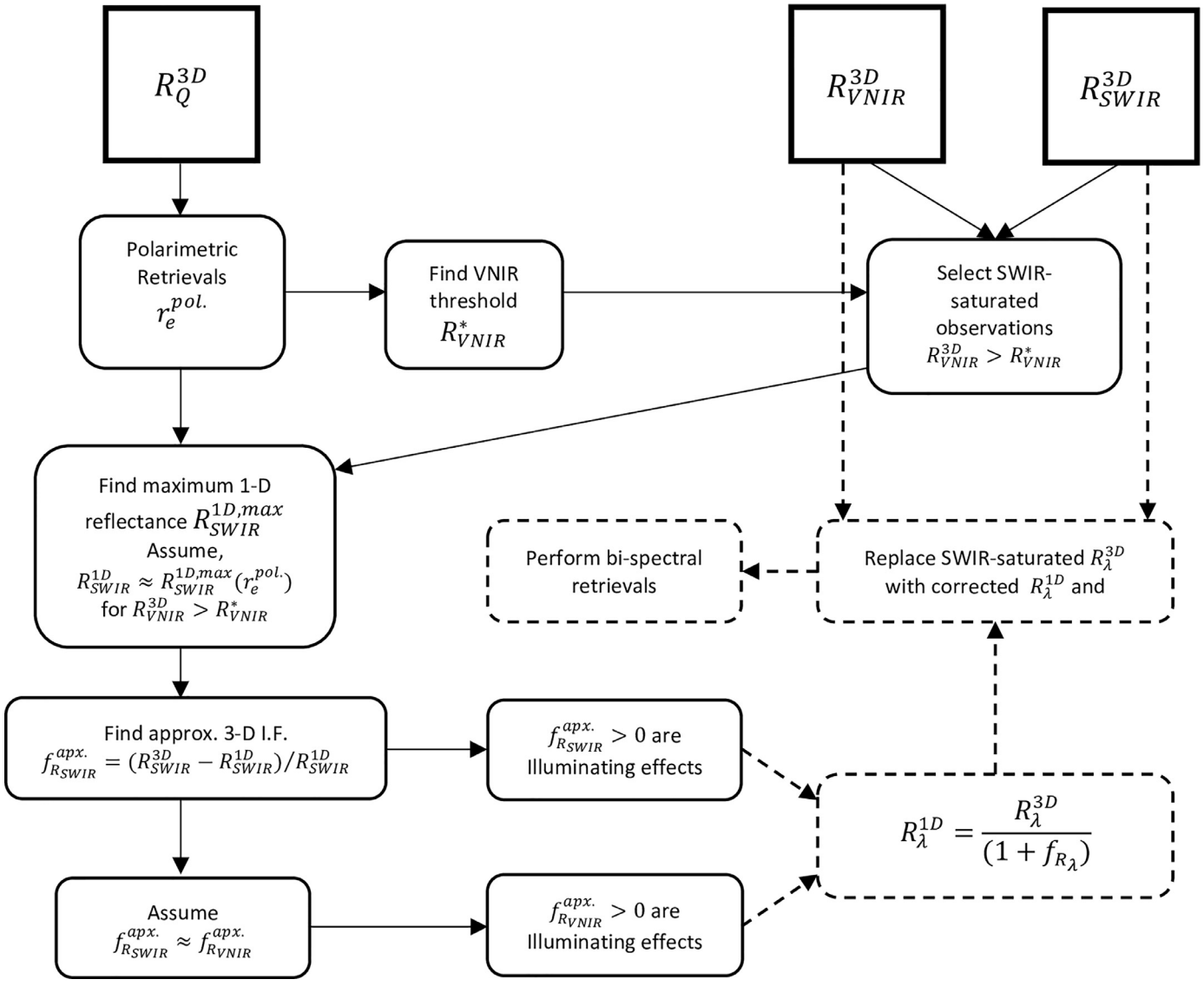

Fig. 6. Flowchart for the practical implementation of the maximum 1-D reflectance method. The detection procedure is shown in solid lines and the COT correction process is shown in dashed lines.

By substituting Eq. (3) into Eq. (2), we can obtain an approximate 3-D effect impact factor $f_{SWIR}^{apx} = (R_{SWIR}^{3D} - R_{SWIR}^{1D,max})/R_{SWIR}^{1D,max}$. Evidently, a positive f_{SWIR}^{apx} indicates illuminating effect. In summary, on the basis of observed and retrieved quantities, i.e., r_e^{pol}, R_{VNIR}^{3D} and R_{SWIR}^{3D} we have developed an algorithm to detect the SWIR-saturated observations that are influenced by the illuminating effect. The performance of this detection algorithm for the fractal cloud case is shown in Fig. 7. As shown in Fig. 7 (a), for the SWIR-saturated pixels (i.e., the pixels where $R_{VNIR}^{3D} > R_{VNIR}^{*}$), $f_{R_{SWIR}}^{apx}$ and the true 3-D effect impact factor ($f_{R_{SWIR}}^{true}$) are almost identical with a correlation coefficient $R^2 \sim 1$, which indicates that our method works extremely well (100% sensitivity with 99.5% accuracy) for detecting the SWIR-saturated pixels (black circles) influenced by the illuminating effect. For comparison purpose, we loosen the requirement for $R_{VNIR}^{3D} > R_{VNIR}^{*}$ and compute the f_{SWIR}^{apx} for all pixels. As expected, $f_{R_{SWIR}}^{apx}$ is systematically smaller than $f_{R_{SWIR}}^{true}$ when considering all pixels. Nevertheless, it is interesting and important to note that when $f_{R_{SWIR}}^{apx}$ is positive the corresponding $f_{R_{SWIR}}^{true}$ is always positive, but the opposite is not true. In other words, a positive $f_{R_{SWIR}}^{apx}$ can be used as a conservative filter (43% sensitivity with 100% accuracy) for detecting the illuminating effect although it has a high missing rate.

So far, our detection algorithm has been focused the SWIR band. An important question remains to be addressed: Does it also work for the VNIR band? To address this question, we compare $f_{R_{SWIR}}^{apx}$ with $f_{R_{VNIR}}^{true}$ in Fig. 7 (b). It is encouraging to see that for 98% of SWIR-saturated pixels (i.e. the pixels where $R_{VNIR}^{3D} > R_{VNIR}^{*}$) (black circles), a positive $f_{R_{SWIR}}^{apx}$ corresponds to a positive $f_{R_{VNIR}}^{true}$. The false detection rate (i.e., a positive $f_{R_{SWIR}}^{apx}$ corresponding to a negative $f_{R_{VNIR}}^{true}$) is only 2%. Moreover, 97% of SWIR-saturated illuminating effects are sensitive to the detections. This result, together with the close correlation between $f_{R_{SWIR}}^{apx}$ and $f_{R_{SWIR}}^{true}$ in Fig. 7 (a), indicates that for pixels with $R_{VNIR}^{3D} > R_{VNIR}^{*}$ an illuminating effect in the SWIR band also implies an illuminating effect in the VNIR band, and they both can be detected using $f_{R_{SWIR}}^{apx}$. However, if we loosen the constraint on $R_{VNIR}^{3D} > R_{VNIR}^{*}$ (gray points in Fig. 7 (b)), 21% of positive $f_{R_{SWIR}}^{apx}$ (i.e., indicative of illuminating effect) would correspond to a negative $f_{R_{VNIR}}^{true}$ (i.e., truly a shadowing effect). In other words, without screening out the SWIR-saturated observations, a

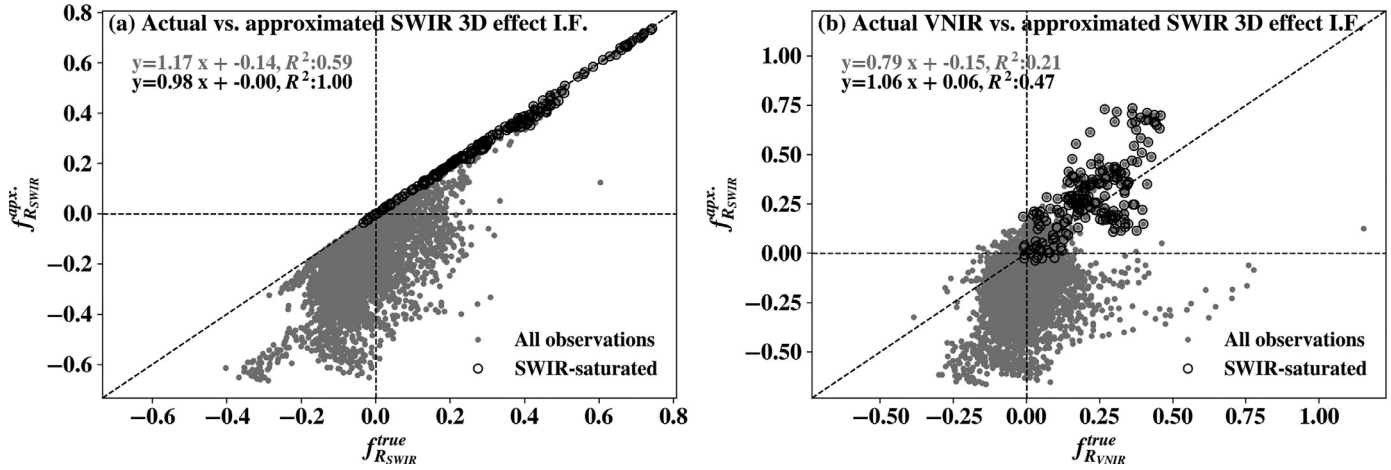

Fig. 7. The correlation of the approximated 3-D effect impact factor of SWIR vs. the actual 3-D effect impact factors of the (a)VNIR and (b) SWIR bands for all (grey points) and SWIR-saturated (i.e. pixels such that $R^{3D}_{VNIR} > R^{*}_{VNIR}$) (black circles) pixels.

simple filter of positive $f^{apx}_{R_{SWIR}}$ for all pixels can lead to 21% false detection. This result indicates that some pixels that influenced by the illuminating effect in the SWIR band (i.e., $R^{3D}_{SWIR} > R^{1D}_{SWIR}$) are influenced by the opposite shadowing effect in the VNIR band (i.e., $R^{3D}_{VNIR} < R^{1D}_{VNIR}$).

6. Explore the possibility of COT bias correction

In the rest of this section, we will try to go one step further and explore the possibility of correcting the COT retrieval bias in the identified pixels. For the reasons discussed in the last section, here we only focus on the SWIR-saturated pixels with $R^{3D}_{VNIR} > R^{*}_{VNIR}$. Assuming that the CER is already known from the polarimetric retrieval, the unbiased COT can be readily estimated from the LUT if the R^{1D}_{VNIR} is known. It follows from Eq. (2) that $R^{1D}_{VNIR} = R^{3D}_{VNIR}/(1 + f_{R_{VNIR}})$. Therefore, the key problem is how to estimate the 3-D effect impact factor for the VNIR band $f_{R_{VNIR}}$. Fig. 7 (b) shows the correlation between the $f^{apx}_{R_{SWIR}}$ and the $f^{true}_{R_{VNIR}}$. As mentioned in the last section, even though the correlation between $f^{apx}_{R_{SWIR}}$ and $f^{true}_{R_{VNIR}}$ for SWIR-saturated observations (black circles) is sufficient to detect VNIR illuminating effects (97% sensitivity with 98% accuracy), $f^{apx}_{R_{SWIR}}$ is not perfectly accurate to approximate $f^{true}_{R_{VNIR}}$ but follows the correct trend with R^2 ~ 0.47. While acknowledging the fact that further investigations are essential to get an accurate relationship between $f^{apx}_{R_{SWIR}}$ and $f^{true}_{R_{VNIR}}$, we approximate that the VNIR and SWIR 3-D effect impact factors are equal to each other based on the trend in Fig. 7 (b) SWIR-saturated pixels (black circles), i.e.,

$$f^{apx.}_{R_{VNIR}} \approx f^{apx.}_{R_{SWIR}} \tag{4}$$

After the VNIR 3-D effect impact factor has been approximated, we can correct SWIR-saturated 3D reflectances of the VNIR band (the pixels where $R^{3D}_{VNIR} > R^{*}_{VNIR}$) for 3-D effects using Eq. (2) ($R^{1D}_{VNIR} = R^{3D}_{VNIR}/(1 + f^{apx}_{R_{VNIR}})$).

Finally, both VNIR and SWIR corrected 3-D reflectances can be provided as input reflectances to the bi-spectral retrievals to get the COT retrievals that are corrected for SWIR-saturated illumination effects.

Fig. 8 summarizes the retrieved COT biases. The x-axis is the bias of the retrieved optical thickness relative to the unbiased retrievals (the retrievals based on 1-D RT-based reflectances) and the y-axis is the probability density function (PDF). The grey line is the retrieved COT biases before the 3-D correction. There are strong positive COT biases even greater than COT = 20 with a mean bias of 1.01. For demonstrational purpose, the dotted line in the figure shows the COT biases of the retrievals after implementing the 3-D correction to all the observations without limiting to the SWIR-saturated observations. In other words, all grey points in Fig. 7 (a) and (b) have been considered to do the corrections in Fig. 8 dotted line. The strong COT biases greater than 20 are corrected but the mean bias becomes 1.81 which is 0.80 greater than the mean bias without any corrections. This is because both $f^{true}_{R_{SWIR}}$ vs. $f^{apx}_{R_{SWIR}}$ and $f^{true}_{R_{VNIR}}$ vs. $f^{apx}_{R_{SWIR}}$ relationships are only reasonable for the SWIR reflectances that have been saturated to reach to the asymptotic maximum ($R^{1D,max}_{SWIR}$). Therefore, in the maximum 1-D reflectance method, we limit the corrections to the SWIR-saturated illuminated pixels (the pixels where $R^{3D}_{VNIR} > R^{*}_{VNIR}$). The black line in Fig. 8 shows the retrieved COT biases after only correcting the 3-D correction for SWIR-saturated observations. The strong illuminating effects of COT retrievals have been detected and corrected with a reasonable accuracy, but the remaining shadowing effects cause a negative bias which will be remained for future studies.

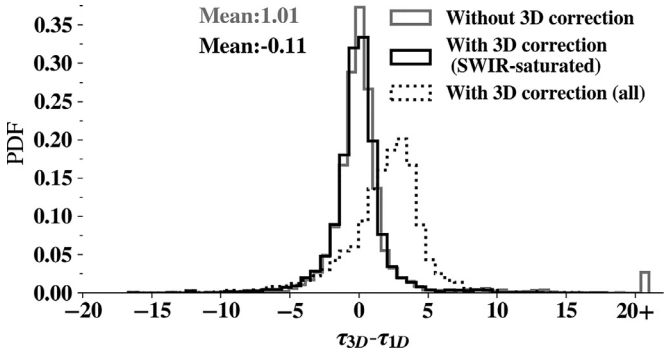

Fig. 8. The summary of COT biases without (grey) and with (black) the 3-D correction based on maximum 1-D reflectance. The x-axis is the bias of retrieved optical thickness relative to the unbiased retrievals (the retrievals based on 1-D RT-based reflectances) and the y-axis is the corresponding probability density function (PDF). Dotted line is the COT bias when the SWIR-saturated constrain has been removed.

7. Requirements on instrument

To implement the maximum 1-D reflectance method in a realistic observational scenario, it is required both radiometric and multiangle polarimetric image of the same cloud target. Despite the gap occurred in the spaceborne polarimetric observations due to the failure of the Glory mission [40], one of the primary instrument of it, Research Scanning Polarimeter (RSP) provides

valuable field measurements of clouds that have been proven to be useful in many studies related to the cloud microphysical retrievals [7,41–43].

RSP measures both total and polarimetric reflectances in 9 spectral bands, 6 VNIR bands and 3 SWIR bands. More importantly it has exceptional angular resolution with 0.8-degree angular intervals within 60 degrees in both forward and backward directions [7] which provide sufficient angular span and resolution to resolve the cloud bow features of the polarized reflectance while providing the radiometric image of the same cloud target. Hence RSP measurements will be a viable observational platform to further investigate the maximum 1-D reflectance method.

Moreover, ESAS (Earth Science and Applications from Space) decadal survey [44] has prioritized the necessity of a multichannel-multiangle polarization imaging radiometer for future climate and air quality studies which will be an encouragement for the further improvements of the maximum 1-D reflectance method towards observational implementations.

8. Discussion and Conclusions

Many studies have been conducted to investigate the 3-D RT effects in passive cloud property retrievals. However, relatively fewer attempts have been made to do pixel-level detections and corrections. From this study, we introduce a novel method called the "maximum 1-D reflectance method" to detect and quantify the 3D RT effects in the bi-spectral cloud property retrievals. The main objective of this study is to explain the theoretical basis and investigate the feasibility of the detection and correction framework based on strictly hypothetical simulated 1-D cloud fields. Rigorous investigations are yet to be done in the future based on more realistic cloud fields (e.g., synthetic cloud fields from large-eddy simulation) and observations (e.g., airborne RSP).

For a given CER, the SWIR reflectance reaches to an asymptotic physical maximum as COT increases. In the maximum 1-D reflectance method, we use this asymptotic physical maximum limit of the SWIR reflectance as a proxy to 1-D SWIR reflectance to detect the 3-D RT effects. Furthermore, we explore the possibility of correcting cloud reflectances, and consequently the COT retrievals for 3-D RT effects. Since the asymptotic maximum value where the SWIR reflectance saturates is chosen as the 1-D reflectance, the corrections that have been made are only accurate for SWIR-saturated observations (pixels). Therefore, a VNIR filtering threshold (R^{*}_{VNIR}) is introduced to select SWIR-saturated observations and the corrections have only been applied to those cases where $R^{3D}_{VNIR} > R^{*}_{VNIR}$.

As shown in Fig. 7 (a) and (b) and explained in Section 5, the maximum 1-D reflectance method is capable of detecting illuminating effects with a remarkable accuracy. For the SWIR-saturated pixels (the pixels where $R^{3D}_{VNIR} > R^{*}_{VNIR}$), maximum 1-D reflectance method has a 100% sensitivity with a 99.5% accuracy for the illuminating effects in the SWIR band and a 97% sensitivity with a 98% accuracy for the illuminating effects in the VNIR band. This is because strong illuminating effects are usually associated with large reflectances which has a high likelihood to cause saturation in the SWIR band. In summary, the maximum 1-D reflectance method can be ideally used to detect illuminating effects in the SWIR-saturated observations. Although the method only sensitive to 43% and 31% of total illumination effects in the SWIR and VNIR bands respectively, it still has a 99% accuracy in the SWIR band and 79% accuracy in the VNIR band illumination effect detection. Hence, maximum 1-D reflectance method could perform as a conservative filter to detect illuminating effects even without constraining to the SWIR-saturated observations, especially in the SWIR band.

Corresponding COT biases before and after implementing the maximum 1-D reflectance method are summarized in Fig. 8. In both without and with SWIR-saturation constraint (dotted and solid black lines respectively), the strong positive COT biases due to the illuminating effects have been corrected. However, R^{1D}_{SWIR} can be approximated by $R^{1D,max}_{SWIR}(r_e^{pol})$ only if the SWIR reflectance being saturated and reached to its asymptotic maximum. Hence, as shown in the dotted line, although the high COT biases have been corrected by the 3-D corrections, the correction that have been applied to the observations where the SWIR reflectance has not been saturated (i.e. $R^{3D}_{VNIR} < R^{*}_{VNIR}$) cause high mean bias. Therefore, in the maximum 1-D reflectance method, we only apply the corrections to the SWIR-saturated pixels (i.e. $R^{3D}_{VNIR} > R^{*}_{VNIR}$ pixels). As shown in the solid black line in Fig. 8, by applying correction only to the SWIR-saturated pixels, maximum 1-D reflectance method can correct the high optical thickness biases in the bi-spectral COT retrievals.

In summary, we introduce a novel method to detect and quantify the 3-D radiative effects in passive cloud property retrievals. In a realistic observational scenario, both polarimetric and radiometric images of the same cloud target will be needed to implement this method. This study only uses strictly hypothetical 1-D cloud fields to explain the main concept and the theoretical basis of the maximum 1-D reflectance method. Rigorous case studies base on more realistic simulated clouds fields and actual observations are yet to be done in the future.

Author statement

Chamara Rajapakshe: Performed the computation, visualization and the prepared the first draft of the manuscript. Zhibo Zhang: conceived the idea, revised and edited the manuscript.

Declaration of Competing interest

The authors declare that they have no known competing financial interests or personal relationships that could have appeared to influence the work reported in this paper.

Acknowledgments

The authors would like to thank the anonymous reviewers for their valuable comments and suggestions. This work is supported by the grant CyberTraining: DSE: Cross-Training of Researchers in Computing, Applied Mathematics and Atmospheric Sciences using Advanced Cyber infrastructure Resources from the US National Science Foundation (grant no. OAC–1730250). The computations in this study were performed at the UMBC High Performance Computing Facility (HPCF). The facility is supported by the US National Science Foundation through the MRI program (grant nos. CNS-0821258 and CNS-1228778) and the SCREMS program (grant no. DMS-0821311), with substantial support from UMBC. ZZ's research is partly supported by NASA grant (80NSSC20K0130) to UMBC.

Supplementary materials

Supplementary material associated with this article can be found, in the online version, at doi:10.1016/j.jqsrt.2020.106920.

References

[1] Nakajima Teruyuki, King Michael D. Determination of the optical thickness and effective particle radius of clouds from reflected solar radiation measurements. part I: theory. J Atmosc Sci 1990;47(15):1878–93. http://journals.ametsoc.org/doi/abs/10.1175/1520-0469%281990%29047%3C1878%3ADOTOTA%3E2.0.CO%3B2.

[2] Cao Changyong, et al. Early on-orbit performance of the visible infrared imaging radiometer suite onboard the suomi national polar-orbiting partnership (s-npp) satellite. IEEE Trans Geosci Remote Sens 2014;52(2):1142–56.

[3] Platnick, Steven et al. 2003. "The MODIS cloud products : algorithms and examples from terra." 41(2): 459–73.

[4] Roebeling RA, Feijt AJ, Stammes P. Cloud property retrievals for climate monitoring: implications of differences between Spinning Enhanced Visible and Infrared Imager (SEVIRI) on METEOSAT-8 and Advanced Very High Resolution Radiometer (AVHRR) on NOAA-17. J Geophys Res Atmos 2006;111(20):1–16.

[5] Bréon, François Marie, and M Doutriaux-boucher. 2005. "A comparison of cloud droplet radii measured from space." 43(8): 1796–1805.

[6] Bréon, François Marie, and Philippe Goloub. 1998. "Cloud droplet effective radius from spaceborne polarization measurements." 25(11): 1879–82.

[7] Alexandrov Mikhail D, et al. Accuracy assessments of cloud droplet size retrievals from polarized reflectance measurements by the research scanning polarimeter. Remote Sens Envir 2012;125:92–111.

[8] Diner DJ, et al. The Airborne Multiangle SpectroPolarimetric Imager (AirMSPI): a new tool for aerosol and cloud remote sensing. Atmos Measurement Techn 2013;6(8):2007–25.

[9] Martins JVanderlei, et al. The harp hyperangular imaging polarimeter and the need for small satellite payloads with high science payoff for earth science remote sensing. Int Geosci Remote Sens Symp (IGARSS) 2018(2018-July): 6304–6307.

[10] Marshak Alexander, et al. ImpaCT OF THREE-DIMENSIONAL RADIATIVE EFFECTS ON SATELLITE RETRIEVALS OF CLOUD DRoplet Sizes. J Geophys Res Atmos 2006;111(9):1–12.

[11] Marshak Alexander, Davis A. 3D radiative transfer in cloudy atmospheres 3d radiative transfer in cloudy atmospheres; 2005.

[12] Várnai Tamás, Davies Roger. Effects of Cloud Heterogeneities on Shortwave Radiation: Comparison of Cloud-Top Variability and Internal Heterogeneity. J Atmos Sci 1999;56(24):4206–24. http://journals.ametsoc.org/doi/abs/10.1175/1520-0469%7B%25%7D281999%7B%25%7D29056%7B%25%7D3C4206%7B%25%7D3AEOCHOS%7B%25%7D3E2.0.CO%7B%25%7D3B2.

[13] Kay JE, et al. Exposing global cloud biases in the Community Atmosphere Model (CAM) using satellite observations and their corresponding instrument simulators. J Clim 2012;25(15):5190–207.

[14] Seethala C, Horváth Ákos. Global assessment of AMSR-E and MODIS cloud liquid water path retrievals in warm oceanic clouds. J Geophys Res Atmos 2010;115(13):1–19.

[15] Chang Ian, Christopher Sundar A. Identifying absorbing aerosols above clouds from the spinning enhanced visible and infrared imager coupled with NASA A-train multiple sensors. IEEE Trans Geosci Remote Sens 2016;54(6):3163–73.

[16] Kaufman Yoram J, et al. The Effect of Smoke, Dust, and Pollution Aerosol on Shallow Cloud Development over the Atlantic Ocean. In: Proceedings of the National Academy of Sciences, 102; 2005. p. 11207–12.

[17] Rosenfeld Daniel, Feingold Graham. Explanation of discrepancies among satellite observations of the aerosol indirect effects. Geophy Res Lett 2003;30(14):1–4.

[18] Loeb Norman G, Davies Roger. Observational evidence of plane parallel model biases: apparent dependence of cloud optical depth on solar zenith angle. J Geophys Res Atmos 1996;101(D1):1621–34.

[19] Marshak Alexander, Davis A, Wiscombe Warren J, Cahalan Robert F. Radiative Smoothing in Fractal Clouds. J Geophys Res 1995;100(D12).

[20] Várnai Tamás, Marshak Alexander. Statistical analysis of the uncertainties in cloud optical depth retrievals caused by three-dimensional radiative effects. J Atmos Sci 2001;58(12):1540–8 doi:10.1175/1520-0469(2001)058%3C1540:SAOTUI%3E2.0.CO%5Cn2.

[21] Zhang Zhibo, et al. Effects of cloud horizontal inhomogeneity and Drizzle on remote sensing of cloud droplet effective radius: case studies based on large-eddy simulations. J Geophy Res Atmos 2012;117(19):1–18.

[22] Zhang Zhibo, Platnick Steven. An Assessment of differences between cloud effective particle radius retrievals for marine water clouds from three MODIS spectral bands. J Geophys Res Atmos 2011;116(20):1–19.

[23] Song Hua, et al. An evaluation of marine boundary layer cloud property simulations in the community atmosphere model using satellite observations: conventional subgrid parameterization versus CLUBB. J Clim 2018;31(6):2299–320.

[24] Takahashi Hanii, et al. An investigation of microphysics and subgrid-scale variability in warm-rain clouds using the A-train Observations and a multiscale modeling framework. J Geophys Res 2017;122(14):7493–504.

[25] Zhang Yuying, et al. Evaluation of clouds in version 1 of the E3SM atmosphere model with satellite simulators. J Adv Model Earth Syst 2019:1253–68.

[26] Di Girolamo Larry, Liang Lusheng, Platnick Steven. A global view of one-dimensional solar radiative transfer through oceanic water clouds. Geophys Res Lett 2010;37(18):1–5.

[27] Zhang Zhibo, et al. Intercomparisons of marine boundary layer cloud properties from the ARM CAP-MBL campaign and Two MODIS cloud products. J Geophy Res 2017;122(4):2351–65.

[28] Várnai Tamás, Marshak Alexander. Observations of three-dimensional radiative effects that influence MODIS cloud optical thickness retrievals. J Atmos Sci 2002;59(9):1607–18.

[29] Cahalan Robert F, et al. The albedo of fractal stratocumulus clouds. J Atmos Sci 1994;51:2434–55.

[30] Davis Anthony B, Marshak Alexander. Reports on Progress in Physics. Reports on Progress in Physics, 73; 2010.

[31] Marshak A, Davis A, Cahalan R, Wiscombe W. Bounded cascade models as nonstationary multifractals. Phys Rev E 1994;49(1):55–69.

[32] Wiscombe Warren J. Mie scattering calculations : advances in technique and fast, vector-speed computer codes. Boulder, Colorado: NCAR Tech, National Center for Atmospheric Research; 1979.

[33] Hansen James E, Travis Larry D. Light scattering in planetary atmospheres. Sp Sci Rev 1974;16(4):527–610.

[34] Emde Claudia, et al. IPRT polarized radiative transfer model intercomparison project – three-dimensional test cases (Phase B). J Quant Spectr Radiat Transf 2018;209:19–44.

[35] Wang Zhen, et al. A novel hybrid scattering order-dependent variance reduction method for Monte Carlo simulations of radiative transfer in cloudy Atmosphere. J Quant Spectr Radiat Transf 2017;189:283–302. doi:10.1016/j.jqsrt.2016.12.002.

[36] Hu YX, et al. δ -Fit: a fast and accurate treatment of particle scattering phase functions with weighted singular-value decomposition least-squares fitting. J Quant Spectr Radiat Transf 2000;65(4):681–90.

[37] Nakajima Teruyuki, Asano Shoji. On the peak truncation approximation of phase function for radia-tive transfer. Sci rep Tohoku Univer Ser. 5, Geophys 1977;24(3):89–102.

[38] Wiscombe WJ. The Delta-M method. J Atmos Sci 1977;30:1408.

[39] Buras Robert, Mayer Bernhard. Efficient unbiased variance reduction techniques for monte carlo simulations of radiative transfer in cloudy atmospheres: The solution. Journal of Quantitative Spectroscopy and Radiative Transfer 2011;112(3):434–47. doi:10.1016/j.jqsrt.2010.10.005.

[40] Mishchenko Michael I, et al. Accurate monitoring of terrestrial aerosol and total solar irradiance: introducing the glory mission. Bull Am Meteorol Soc 2007.

[41] Alexandrov Mikhail D, et al. Characterization of cloud microphysical parameters using airborne measurements by the research scanning polarimeter. In: AIP Conference Proceedings; 2013.

[42] Alexandrov Mikhail D, et al. Liquid water cloud properties during the Polarimeter Definition Experiment (PODEX). Remote Sensing of Environment 2015.

[43] Alexandrov Mikhail D, Cairns Brian, Mishchenko Michael I. Rainbow Fourier Transform. J Quant Spectr Radiat Transf 2012;113(18):2521–35. doi:10.1016/j.jqsrt.2012.03.025.

[44] NASEM. Thriving on our changing planet: a decadal strategy for earth observation from space. Washington, DC: The National Academies Press; 2018 https://www.nap.edu/read/24938/chapter/1.